Response of patients with melanoma to immune checkpoint blockade – insights gleaned from analysis of a new mathematical mechanistic model

N. Tsur [a], Y. Kogan [a,b], M. Rehm [c,d], Z. Agur [a,b,*]

[a] *Optimata Ltd., Zichron Ya'akov St., 20, Tel Aviv 6299920, Israel*
[b] *Institute for Medical BioMathematics (IMBM), Hate'ena St. 10, Bene-Ataroth 6099100, Israel*
[c] *Institute of Cell Biology and Immunology, University of Stuttgart, Allmandring 31, Stuttgart D-70569, Germany*
[d] *Stuttgart Research Center Systems Biology, University of Stuttgart, Nobelstrasse 15, Stuttgart D-70569, Germany*

ARTICLE INFO

ABSTRACT

Immune checkpoint inhibitors (ICI) are becoming widely used in the treatment of metastatic melanoma. However, the ability to predict the patient's benefit from these therapeutics remains an unmet clinical need. Mathematical models that predict melanoma patients' response to ICI can contribute to better informed clinical decisions. Here, we developed a simple mathematical population model for pembrolizumab-treated advanced melanoma patients, and analyzed the local and global dynamics of the system. Our results show that zero, one, or two steady states of the mathematical system exist in the phase plane, depending on the parameter values of individual patients. Without treatment, the simulated tumors grew uncontrollably. At increased efficacy of the immune system, *e.g.,* due to immunotherapy, two steady states were found, one leading to uncontrollable tumor growth, and the other resulting in tumor size stabilization. Model analysis indicates that a sufficient increase in the activation of CD8+ T cells results in stable disease, whereas a significant reduction in T-cell exhaustion, another process contributing CD8+ T cell activity, temporarily reduces the tumor mass, but fails to control disease progression in the long run. Importantly, the initial tumor burden influences the response to treatment: small tumors respond better to treatment than larger tumors. In conclusion, our model suggests that disease progression and response to ICI depend on the ratio between activation and exhaustion rates of CD8+ T cells. The analysis of the model provides a foundation for the use of computational methods to personalize immunotherapy.

© 2019 Elsevier Ltd. All rights reserved.

1. Introduction

Advanced melanoma is the most deadly skin cancer. In 2015, 351,880 new cases were diagnosed worldwide, and 59,782 deaths were reported (Karimkhani et al., 2017). For 2018, a total of 91,279 new cases, and 9,320 deaths are expected in the United States (Siegel et al., 2018). Most early-detected melanomas are curable by resection (Terushkin and Halpern, 2009), whereas metastatic disease requires systemic treatment. Melanoma cells can stimulate host immunity by their high mutation burden, enabling recognition as non-self-antigens and activation of antigen presenting cells (APCs). The latter stimulate CD8+ T cells to differentiate into memory and cytotoxic effector CD8+ T cells (Dustin, 2014; Gattinoni et al., 2012). Melanoma can also suppress host immunity by expressing ligands which bind to regulatory receptors on activated immune cells - cytotoxic T lymphocyte-associated protein 4 (CTLA-4) and programmed cell death 1 (PD-1) - and inhibit immune activity (Butte et al., 2007; Chapon et al., 2011; Walker and Sansom, 2011).

Treatment of melanoma has been revolutionized with the approval of ICIs. For example, treatments based on pembrolizumab and nivolumab, inhibitors of the immune checkpoint receptor, programmed cell death 1 (PD-1), greatly improved prognosis in metastatic disease (Robert et al., 2015). However, even though ICIs can induce durable response in some patients (Ott et al., 2013; Prieto et al., 2012), the overall response rate to these drugs is still modest (Hamid et al., 2013; Hodi et al., 2010) and reliable markers to predict treatment efficacy are still under development (Wang et al., 2012; Weide et al., 2016)

The complex interplay of cancer cells and the host immune system, as affected by immunotherapy, renders the reasoning of treatment causality difficult. Having the capacity to succinctly integrate

this interplay in one coherent framework, and enable its analysis, mathematical models may become instrumental in predicting the interactive dynamics of host immunity, cancer progression and immunotherapy, thereby providing a new powerful tool for treatment personalization. Mathematical models have been previously employed for studying the interactions of cancer with the immune system, for investigating the response to different immunotherapies, and for patient-specific regimen personalization (Adam and Bellomo, 2012; Agur et al., 2016; d'Onofrio, 2005; d'Onofrio, 2008; Eftimie et al., 2016; Eladdadi and Radunskaya, 2014; Foryś et al., 2016; Kogan et al., 2012; Kronik et al., 2010). While suited to their specific aims, none of these models included cellular immunity in a way that enables analysis of treatment by ICI. In particular, previous models did not address the recently discovered effects of Effector T cell exhaustion on the treatment. The elucidation of these effects are crucial for evaluating the efficacy of ICI and, therefore, are introduced into the mathematical model developed and analyzed in this work.

In this study, we developed a mathematical mechanistic model for the interactions of melanoma cells with the host immune system, and analyzed the effects ICIs have on this interplay. Our study indicates that different potential immunotherapy strategies, which are expected to enhance the efficacy of CD8+ T cells, result in distinct tumor dynamics and disease fates.

2. Methods

2.1. Mathematical model

Our mathematical model simplifies the overall system to its main driving forces, namely, melanoma cells, antigen-presenting cells (APCs), and effector CD8+ T cells. It takes into account the following assumptions about the involved dynamics:

1. Mutated tumor cells express non-self-antigens and activate APCs. The number of activated functional APCs, denoted A, depends on the tumor immunogenicity (Chen et al., 1994; Rizvi et al., 2015; Schumacher and Schreiber, 2015; Snyder et al., 2014), which is reflected in the activation rate of APCs, (α_A). The activation of APCs increases with tumor load, towards saturation. The number of tumor cells required to reach half of the maximal activation rate of APCs is denoted by the coefficient b.
2. Functional APCs die with a rate μ_A.
3. Functional APCs activate effector antigen-specific CD8+ T cells (T) (Dustin, 2014; Ott et al., 2013; Dustin, 2002), at a rate α_e.
4. Effector CD8+ T cells eliminate tumor cells (Ott et al., 2013; Cipponi et al., 2011).
5. Effector CD8+ T cells are eliminated at a rate, μ_e. This term accounts for the cell death and exhaustion due to the encounter with tumor cells and regulatory cells. For simplicity, we assume that this rate does not depend on the tumor size.
6. The number of tumor cells at any moment, M, is determined by their net growth rate (γ_{mel}) and the rate of elimination by effector CD8+ tumor lymphocytes (T), denoted ν_{mel}. Their death rate due to the immune system is assumed to reach saturation in M, depending on the coefficient g.
7. Administration of ICI treatment increases the activation rate of CD8+ T cells α_e, and reduces the elimination rate of CD8+ T cells, μ_e.

A graphical presentation of the modelled components and their interactions is given in Fig. 1.

Based on the above assumptions, we formulated the following ODE model:

a) $\quad \dfrac{dA}{dt} = \alpha_A \cdot \dfrac{M}{M+b} - \mu_A \cdot A,$

b) $\quad \dfrac{dT}{dt} = \alpha_e \cdot A - \mu_e \cdot T,$

c) $\quad \dfrac{dM}{dt} = \gamma_{mel} \cdot M - \upsilon_{mel} \cdot \dfrac{T \cdot M}{M+g}.$ $\qquad$ (1)

Eq. (1a) describes the dynamics of APCs in the system, where the first term on the right-hand side (r.h.s) stands for the activation of APCs by cancer cells, and the second term stands for their death. Eq. (1b) describes the dynamics of effector CD8+ T cells in the system. The first term on the r.h.s. corresponds to activation of effector CD8+ T cells by APCs, and the second term denotes the death of effector cells. Eq. (1c) describes tumor growth, with the first term on the r.h.s. standing for the tumor growth rate, and the second term denoted destruction of tumor cells by effector CD8+ T cells.

2.2. Parameter definition and estimation

Realistic parameter ranges for model simulations were estimated from published experimental and clinical data, as summarized in Table 1.

The following paragraphs describe the parameter estimation methods in more detail.

2.2.1. α_A and b: activation of antigen presenting cells (APCs) by tumor cells

These two parameters are related to activation of APCs by tumor cells. For their estimation we considered dendritic cells (DCs) solely, since they constitute the majority of APCs and play the main role in CD8+ T cells activation. Activation rate of functional DCs depends on the immunogenicity of the tumor, in terms of antigen availability, as well as DCs maturation, determined here by migration rate DCs into the Lymph Nodes (LNs). The level of antigen, which varies among patients, is proportional to the number of antigen-expressing melanoma cells.

Both α_A and b were estimated from co-culture experiments of DCs with irradiated melanoma cells (Barrio et al., 2012; Von Euw et al., 2007). The relation of these parameters to DCs activation is derived from Eq. (1a):

$$\frac{dA}{dt} \approx \frac{\%phago \cdot \%migration \cdot A_0}{\Delta t} \approx \alpha_A \cdot \frac{M_0}{M_o + b}. \qquad (2)$$

The variables A_0 and M_0 denote the number of co-cultured APCs and melanoma cells, respectively. The variable M_0 is the number of melanoma cells, which is held constant for simplicity, %phago denotes the calculated rate of melanoma cells phagocytosis by APCs, %migration is migration rate of APCs from the skin to LNs, which is assumed as an indicator of APCs maturation, and estimated around 2% (de Vries et al., 2003; de Vries et al., 2005). Lastly, Δt is the duration of the co-culture experiment.

The co-culture results of human melanoma cell lines with APCs from healthy donors are summarized in Table 2.

Substitution of the data in into Eq. (2) yields

$$\alpha_A = 1.161 \cdot 10^3 - 2 \cdot 986 \cdot 10^3 \left[\frac{cells}{d} \right],$$

$$b = 3.704 \cdot 10^4 - 1 \cdot 476 \cdot 10^5 \ [cells]. \qquad (3)$$

For the model analysis we used the average value of b, which is 9.233×10^4 cells.

Table 1
Estimated parameter values.

Model parameter	Definition	Estimated value/range	Units	Source
α_A	Activation rate of APCs	1.161×10^3–2.986×10^3	cells/d	(Barrio et al., 2012; Von Euw et al., 2007)
b	Number of tumor cells, required for reaching half of the maximal APC activation rate	3.704×10^4–1.476×10^5	Cells	(Barrio et al., 2012; Von Euw et al., 2007; Lee et al., 2007)
μ_A	Death rate of APCs	0.2310	d^{-1}	(Kamath et al., 2000)
α_e	Activation rate of naïve antigen-specific CD8+ T cells	0.8318	d^{-1}	(Bossi et al., 2013)
μ_e	Death rate of Effector CD8+ T cells	0.1777	d^{-1}	(Taylor et al., 1999)
γ_{mel}	Net growth rate of tumor cells	0.003269–0.08664	d^{-1}	(Carlson, 2003)
υ_{mel}	Innate death rate of tumor cells by effector CD8+ T cells	0.1245	d^{-1}	(Kuznetsov, 1990; Kuznetsov et al., 1992; Kuznetsov et al., 1994)
g	Number of tumor cells, at which the elimination rate reaches half of its maximal value	2.019×10^7–$1 \bullet 10^8$	cells	(Kronik et al., 2010; Kuznetsov et al., 1994)

Table 2
Experimental results of human APCs and melanoma cells co-culture. The parameters are defined under Eq. (2). (a) Estimated number of cells. (b) The experiment was performed in wells, containing 3×10^5/ml DCs. The volume of each well was 3.5 ml. (c) Mostly MART-1+ melanoma cells.

A_0: M_0 ratio	A_0 [cells]	M_0 [cells]	%phago	Δt [d]	Reference
3:1	1×10^5 (a)	3.33×10^4	55	2	(Von Euw et al., 2007)
3:1	1.05×10^6 (b)	3.5×10^5 (c)	10–20	2	(Barrio et al., 2012)

2.2.2. μ_A: death rate of APCs

The death rate of DCs was estimated from the half-life time of splenic murine DCs, which is three days (Kamath et al., 2000). Accordingly, $\mu_A = \frac{\ln(2)}{3} = 0.2310\ d^{-1}$.

2.2.3. α_e: activation rate of antigen-specific CD8+ T cells

According to (Bossi et al., 2013), the half-life of binding between a T cell and its conjugant epitope on an APC is 20 h. This corresponds to an activation rate $\alpha_e = \frac{\ln(2)}{\frac{20}{24}} = 0.8318\ d^{-1}$.

2.2.4. μ_e: exhaustion rate of effector CD8+ T cells

We calculated the exhaustion rate of effector CD8+ T cells from their half-life time, τ: $\mu_e = \frac{ln(2)}{\tau}$.

Our estimation of the half-life time is based on experimental examination of different immunogens as triggers for the T cell activation. We assume that the influence of the immunogen nature on T cells life span is negligible. Taylor et al. (1999) estimated a lifetime of 3.9 days for effector T cells in peripheral blood of patients with human T-cell leukemia virus type 1 (HTLV-1). This corresponds to an exhaustion rate of $\mu_e = 0.1777\ d^{-1}$.

2.2.5. γ_{mel}: net growth rate of tumor cells

In our model, we assume an exponential cancer growth (Eq. (1c)). γ_{mel} is calculated from the doubling time of melanoma metastasis: $\gamma_{mel} = \frac{\ln(2)}{\Delta t}$, where Δt is the doubling time. Carlson (2003) estimated the tumor doubling time from clinical
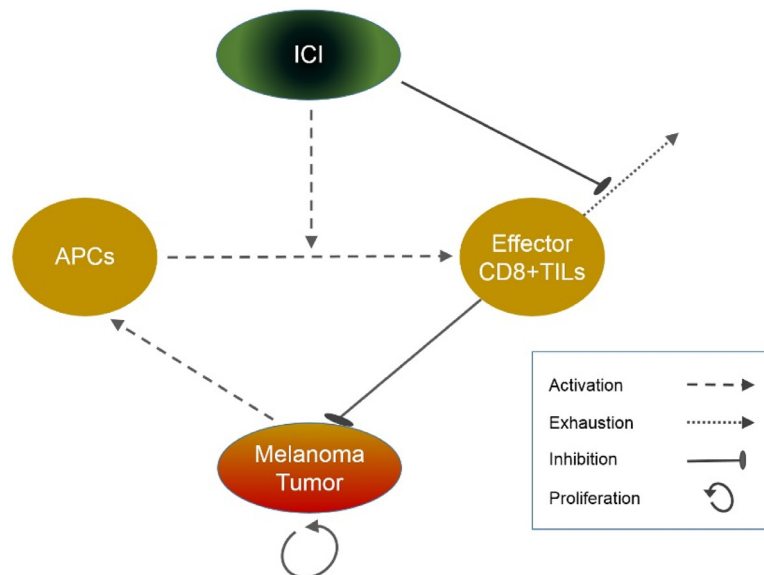

Fig. 1. A simple model for the dynamics of the melanoma tumor (red-mustard), the cellular immune system (APCs and Effector CD8+ TILs), and the immune checkpoint inhibitor (ICI; green). The model is based on the following assumptions: tumor cells stimulate antigen-presenting cells (APCs; mustard, left), depending on the tumor immunogenicity; functional APCs activate Effector CD8+ T cells (mustard; right), which may infiltrate into the tumor and eliminate tumor cells (TILs, right); Effector CD8+ TILs become exhausted, independently of tumor cell elimination; tumor growth is determined by its net growth rate and by the rate of its destruction by Effector CD8+ TILs. Treatment by ICI prolongs activation of effector TILs, and reduces their exhaustion. Ellipses represent the dynamic variables of the model, while arrows represent the interactions between them (see box).

Table 3
Numerical description of the phase planes shown in Fig. 6.

Figure	Value of the changed parameter[*]	Range of initial number of tumor cells (M^0)	Initial number of immune cells (perturbation from a quasi-steady state) [**]
(a)	-	10–10^9	1
(b)	$\alpha_e = 0.8318 \cdot 557.22\, d^{-1}$ [***]	10^4–10^8	(0.5, 2.5)
(c)	$\alpha_e = 0.8318 \cdot 10^3 [d^{-1}]$	10^4–10^9	(0.5, 1.9)
(d)	$\mu_e = 0.1777 \cdot 10^{-3} [d^{-1}]$	10^4–10^8	1
(e)	$\gamma_{mel} = 0.0449 \cdot 10^{-3} [d^{-1}]$	10^4–10^9	(0.5, 1.5)

[*] Relative to the reference value from Table 1.

[**] The initial conditions of immune cells were calculated according to Eq. (5), by assuming that the number of immune cells adjusts itself rapidly to any change in the number of tumor cells. In order to determine the dynamic patterns over a larger range of initial conditions, we perturbed the initial number of cells from the ones calculated in Eq. (5) by multiplying all the immune cells by a constant, specified here for each subfigure in Fig. 6.

[***] This value for α_e satisfies the condition for a single FP $\alpha_e \cdot (\frac{\nu_{mel} \cdot \alpha_A}{\gamma_{mel} \cdot \mu_e \cdot \mu_A}) = b + g + 2 \cdot \sqrt{b \cdot g}$ (see Eq. (13)).

data of three patients as $\Delta t = 8 - 212\, d$. The corresponding growth rate is $0.003269 < \gamma_{mel} < 0.086643$. This is a few orders smaller than the tumor growth rate calculated from *ex vivo* murine models. In addition, (Joseph et al., 1971) measured an average doubling time of 32 days in three patients with pulmonary melanoma metastasis. The resulting tumor growth rate is $\gamma_{mel} < 0.02166\, d^{-1}$. For the model analysis we took the average tumor growth rate of $0.04496\, d^{-1}$.

2.2.6. g: Michaelis–Menten constant of effector-tumor cells interaction

We adapted the value $g = 2.019 \cdot 10^7\, cells$ from (Kuznetsov, 1990; Kuznetsov et al., 1992; Kuznetsov et al., 1994), based on BCL-1 lymphoma cells transplanted in spleens of chimeric mice, and (Kronik et al., 2008) who estimated a value of $g = 10^8\, cells$. For the model analysis we considered the average value of $g = 6.01 \cdot 10^7\, cells$.

2.3. Software

Numerical analyses and simulations were performed using the ode15s Runge-Kutta ODE solver of Matlab R2016a (The Mathsworks, UK).

3. Results

3.1. Defining a biologically relevant domain for model analysis

Asymptotic solutions for the system defined in Eq. (1) are of interest, since they indicate the potential fates of the system. For example, a positive, steadily growing number of cancer cells over time suggests inability to cure the disease. Additional potential solutions include, for instance, a decrease in the number of tumor cells down to a constant amount, indicating shrinkage and tumor stabilization thereafter. Further solutions may present oscillations that might indicate alternating periods of tumor shrinkage and growth.

Assuming $A(t_0) \geq 0$, $T(t_0) \geq 0$, $M(t_0) \geq 0$, solutions for Eq. (1) exist for any $t > t_0$, and the domain defined by:

$$0 \leq A \leq \frac{\alpha_A}{\mu_A},$$
$$0 \leq T \leq \frac{\alpha_e \cdot \alpha_A}{\mu_e \cdot \mu_A},$$
$$0 \leq M. \tag{4}$$

is invariant (i.e., if a trajectory has initial values inside this domain, it will remain there). To see this, note that from Eq. (1) we have the following two differential inequalities

$$-\mu_A \cdot A \leq \frac{dA}{dt} \leq \alpha_A - \mu_A \cdot A,$$

$$-\mu_e \cdot T \leq \frac{dT}{dt} \leq \alpha_e \cdot A - \mu_e \cdot T.$$

From the former, by the comparison theorem for ODEs it follows that $A(t)$ is bounded from above and below by the trajectories of the equations $\dot{x} = -\mu_A \cdot x$ and $\dot{x} = \alpha_A - \mu_A \cdot x$, with the same initial value, correspondingly. Hence, if $A(t_0) \in [0, \frac{\alpha_A}{\mu_A}]$, then for each $t > t_0$, $A(t) \in [0, \frac{\alpha_A}{\mu_A}]$. Similar reasoning, taking into account the bounds obtained for $A(t)$ gives the bounds for $T(t)$. Finally, we have $\dot{M} \geq (\gamma_{mel} - \nu_{mel} \cdot T) \cdot M$, from which it follows by comparison that if $M(t_0) \geq 0$, then $M(t) \geq 0$ for any $t \geq t_0$.

In the following, we limit the analysis to the biologically relevant domain, defined in Eq. (4), additionally assuming that all system parameters are positive.

3.2. Multiple steady states and their stability analysis

Theoretical and numerical analysis of the model enables to determine the number of steady states in the system, and the conditions for their stability, as well as to identify the critical bifurcation points. The steady states and the critical bifurcation points can pinpoint parameter ranges for which treatment with ICIs can turn persistent tumor growth in an untreated host into conditions under which the immune system can control the disease. We therefore determined the fixed points (FPs) in Eq. (1) by nullifying the derivatives and solving the resulting algebraic system, obtaining one trivial solution, for $M^* = 0$ and two non-trivial solutions, for $M^* > 0$:

$$A = \frac{\alpha_A}{\mu_A} \cdot \frac{M}{M + b},$$
$$T = \frac{\alpha_e}{\mu_e} \cdot A,$$
$$M \cdot [\gamma_{mel} \cdot (M + g) - \nu_{mel} \cdot T] = 0. \tag{5}$$

3.2.1. Immune cells are not activated in a tumor-free state

In order to analyze the tumor dynamics around the trivial steady state, we determined the stability of the associated steady state solution of Eq. (1). Substituting $M = 0$ in Eq. (5) reflects the case of a tumor-free host. This yields the FP $(A^*, T^*, M^*) = (0, 0, 0)$, which indicates correctly that for this condition tumor-specific immune cells are not activated.

The Jacobi matrix of this FP is:

$$\begin{pmatrix} -\mu_A & 0 & \frac{\alpha_A}{b} \\ \alpha_e & -\mu_e & 0 \\ 0 & 0 & \gamma_{mel} \end{pmatrix}$$

The characteristic polynomial of this matrix is:

$$P(\lambda) = (\mu_A + \lambda) \cdot (\mu_e + \lambda) \cdot (-\gamma_{mel} + \lambda). \tag{6}$$

The eigenvalues of the Jacobi matrix are $(-\mu_A, -\mu_e, \gamma_{mel})$. Since not all real parts of the matrix are negative, the FP $(A^*, T^*, M^*) = (0, 0, 0)$ is unstable. From this we conclude that if a tumor exists at time zero in the model, namely $M(0) > 0$, it will not disappear, and, plausibly, the number of tumor cells will diverge from zero.

3.2.2. Steady states in a tumor-positive scenario can indicate disease progression or treatment efficacy

Next we studied the conditions under which steady states of the system can be identified in the presence of tumor. A steady state solution can be obtained by solving Eq. (5) for $M \neq 0$. Substitution of the expression for T in the expression for M in Eq. (5) yields

$$M = \frac{\nu_{mel}}{\gamma_{mel}} \cdot \frac{\alpha_e}{\mu_e} \cdot \frac{\alpha_A}{\mu_A} \cdot \frac{M}{M+b} - g. \tag{7}$$

By defining $\bar{K} \equiv \frac{\nu_{mel} \cdot \alpha_e \cdot \alpha_A}{\gamma_{mel} \cdot \mu_e \cdot \mu_A}$ for convenience, Eq. (7) becomes

$$M^2 + (b + g - \bar{K}) \cdot M + b \cdot g = 0. \tag{8}$$

The parameter $\bar{K}$ represents the ratio between the efficacy of the immune response and the tumor growth capacity. Solving Eq. (8) yields M at steady state, M^*:

$$M^* = \frac{\bar{K} - (b+g) \pm \sqrt{(b + g - \bar{K})^2 - 4b \cdot g}}{2} \equiv M^{\pm}. \tag{9}$$

The two roots $M^{\pm}$ represent two different FP values for the number of cancer cells. The number of immune cells in steady state are obtained from substitution of Eq. (9) in Eq. (5):

a) $A^* = \frac{\alpha_A}{\mu_A} \cdot \frac{M^{\pm}}{M^{\pm} + b} \equiv A^{\pm},$

b) $T^* = \frac{\alpha_e}{\mu_e} \cdot A^{\pm}. \tag{10}$

Depending on the value of $\bar{K}$, Eq. (8) can have zero, one or two real positive solutions. A necessary condition on $\bar{K}$, for Eq. (8) to have real positive roots is given by

$$\bar{K} > (b + g). \tag{11}$$

By nullifying the discriminant of M^* in Eq. (9), we obtain the condition on $\bar{K}$ for a single root, that is, a single FP:

$$\bar{K}_{1,2} = b + g \pm 2\sqrt{b \cdot g} = \left(\sqrt{b} \pm \sqrt{g}\right)^2. \tag{12}$$

$\bar{K}_{1,2}$ are the values of $\bar{K}$, which correspond to a single FP.

The system in Eq. (1) has one real positive FP (PFP), when conditions (11) and (12) are satisfied i.e., when

$$\bar{K} = \left(\sqrt{b} + \sqrt{g}\right)^2. \tag{13}$$

The discriminant in Eq. (9) is positive when $\bar{K} < (\sqrt{b} - \sqrt{g})^2$, or $\bar{K} > (\sqrt{b} + \sqrt{g})^2$. Together with the positivity condition in Eq. (11), Eq. (8) has two real positive roots, that is, two PFPs, when:

$$\bar{K} > \left(\sqrt{b} + \sqrt{g}\right)^2. \tag{14}$$

From this we conclude that different values of $\bar{K}$ impose different stability patterns on the system, including a possible saddle-node bifurcation, when two FPs collide and disappear. To visualize this, we rewrite Eq. (8) in the form

$$(M + b) \cdot (M + g) = \bar{K} \cdot M. \tag{15}$$

The left-hand side (l.h.s.) of Eq. (15) is a parabola and its r.h.s. is a straight line. In Fig. 2, both sides of Eq. (15) are plotted against each other for different parameter values. Intersections of the lines mark the FPs, and their number depends on the values of $\bar{K}$, b and g. For $\bar{K} > (\sqrt{b} + \sqrt{g})^2$, the lines intersect twice on $M > 0$, resulting in two PFPs (dashed line). As $\bar{K}$ decreases, the intersections approach each other, until they collide when $\bar{K} = (\sqrt{b} + \sqrt{g})^2$ (grey solid line). The corresponding system has a single FP. For

$\bar{K} < (\sqrt{b} + \sqrt{g})^2$, the lines in Eq. (15) do not intersect on $M > 0$ and therefore Eq. (8) has no positive solutions (dashed-dotted line).

The value of $\bar{K}$ for which the system has a single FP (see Eq. (13)), is $\bar{K} \approx 6.5 \cdot 10^7$ cells (Table 1). As demonstrated in Fig. 3, for smaller $\bar{K}$, no PFPs exist, and as will be shown late, the corresponding tumors grow uncontrollably. For larger values of $\bar{K}$, the system has two PFPs, biologically corresponding to tumor shrinkage or disease stabilization, due to immune control, *i.e.*, by ICI treatments.

3.2.3. Tumor PFPs can be locally stable under increased activation or reduced exhaustion rates of CD8+ T cells, and when the tumor growth rate is low

To learn about the stability properties of the PFPs of Eq. (1), we first studied their local stability. This included calculation of the eigenvalues of the Jacobi matrix of the system, as shown below:

$$\begin{pmatrix} -\mu_A & 0 & \frac{\alpha_A \cdot b}{(M^*+b)^2} \\ \alpha_e & -\mu_e & 0 \\ 0 & -\frac{\nu_{mel} \cdot M^*}{M^*+g} & \gamma_{mel} - \frac{\nu_{mel} \cdot T^* \cdot g}{(M^*+g)^2} \end{pmatrix}$$

Note that this matrix depends on the steady state values: (A^*, T^*, M^*).

The determinant of $\hat{J} - \lambda \hat{I}$ is a 3rd order characteristic polynomial:

$$P(\lambda) = (\mu_A + \lambda) \cdot (\mu_e + \lambda) \cdot \left[\frac{\nu_{mel} \cdot g \cdot T^*}{(M^* + g)^2} - \gamma_{mel} + \lambda \right]$$
$$+ \alpha_A \cdot \alpha_e \cdot \nu_{mel} \cdot \frac{b}{(M^* + b)^2} \cdot \frac{M^*}{M^* + g}. \tag{16}$$

By defining $\bar{\Delta}_1 \equiv \gamma_{mel} - \frac{\nu_{mel} \cdot g \cdot T^*}{(M^*+g)^2}$ and $\bar{\Delta}_2 \equiv \alpha_A \cdot \alpha_e \cdot \nu_{mel} \cdot \frac{b}{(M^*+b)^2} \cdot \frac{M^*}{M^*+g}$, Eq. (16) becomes

$$P(\lambda) = (\lambda + \mu_A) \cdot (\lambda + \mu_e) \cdot (\lambda - \bar{\Delta}_1) + \bar{\Delta}_2. \tag{17}$$

Further simplification of $\bar{\Delta}_1$ and $\bar{\Delta}_2$ is achieved by substituting T^* from Eq. (5b), $\bar{K}$, and Eq. (15) into Eq. (17):

a) $\bar{\Delta}_1 = \gamma_{mel} \cdot \frac{M^*}{M^*+g},$

b) $\bar{\Delta}_2 = \gamma_{mel} \cdot \mu_A \cdot \mu_e \cdot \frac{b}{M^*+b}. \tag{18}$

The values of $\bar{\Delta}_1$ and $\bar{\Delta}_2$ are limited to the following ranges (Eq. (19)), considering that $M^* \geq 0$ (Eq. (4)).

a) $0 < \bar{\Delta}_1 < \gamma_{mel},$

b) $0 < \bar{\Delta}_2 < \gamma_{mel} \cdot \mu_e \cdot \mu_A. \tag{19}$

A FP is locally asymptotically stable (LAS) if all the real parts of its corresponding eigenvalues are negative. To study the signs of the real parts, we graphically analyzed Eq. (17) for different values of $\bar{\Delta}_1$ and $\bar{\Delta}_2$ (Fig. 4).

Claim 1. Given that all the eigenvalues of a PFP of Eq. (1) are real, there exists $\bar{\Delta}_{2_{crit}}$ such that this point is LAS if

a) $\bar{\Delta}_2 > \bar{\Delta}_{2_{crit}},$

b) $\left. \frac{dP(\lambda, \bar{\Delta}_2 = 0)}{d\lambda} \right|_{\lambda=0} > 0. \tag{20}$

Proof of Claim 1. To prove sufficiency, assume that Eq. (20b) holds. When $\bar{\Delta}_2 = 0$, all the roots of the polynomial in Eq. (17) are real. As shown in Fig. 4a, the largest zero is positive and the rest are negative. A positive value of $\bar{\Delta}_2$ shifts the polynomial graph upwards, leading to a decrease in the value of the largest root, until it changes sign (Fig. 4b). As a result, the corresponding FP becomes LAS. The critical value of $\bar{\Delta}_2$, at which the largest root
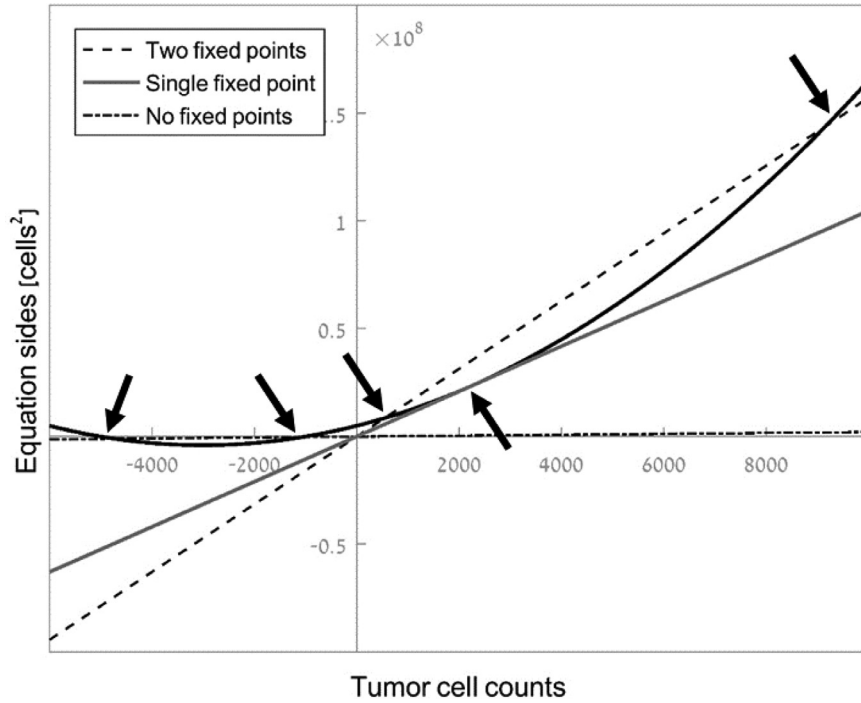
Fig. 2. Existence and number of PFPs depends on the value of $\bar{K}$. This Fig. is a graphical analysis of Eq. (15). The black solid curve represents the left-hand side (l.h.s.) of the equation, the others represent the right-hand side (r.h.s.) of Eq. (15) for different values of $\bar{K}$. The arrows mark the intersections between the r.h.s. and l.h.s. of Eq. (15). The grey solid line demonstrates the case of a single tangential intersection of the equation sides (for $\bar{K} = (\sqrt{b} + \sqrt{g})^2$). This corresponds to a single solution, i.e., one PFP. If the r.h.s. line has a steeper slope than the grey solid line, two intersections are obtained, and the system has two PFPs. In case the r.h.s. line has a lower slope than the grey line (dashed-dotted line), the system has no PFPs.
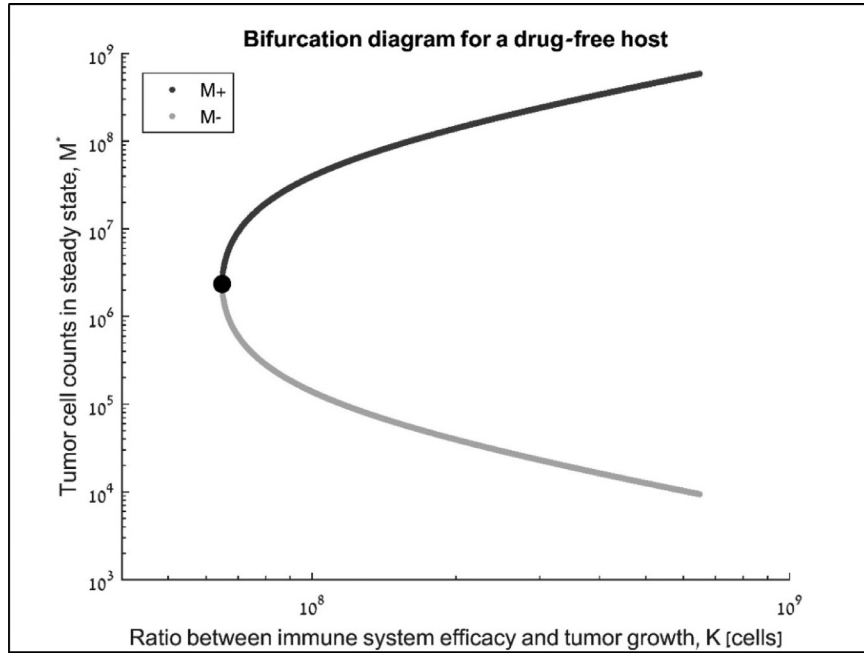

Fig. 3. Bifurcation diagram displaying positive steady states of the Eq. (1). The number of cancer cells in steady state (M_{el}^*) is plotted versus the parameter $\bar{K} \equiv \frac{\nu_{mel} \cdot \alpha_e \cdot \alpha_A}{\gamma_{mel} \cdot \mu_e \cdot \mu_A}$. As shown in Fig. 2, the number of FPs depends on the value of $\bar{K}$. Under the estimated parameters in Table 1 and according to Eq. (13), the system has a single PFP when $\bar{K} \approx 6.5 \cdot 10^7 \, \textbf{cells}$, with $M_{el}^* = 2.35 \cdot 10^6 \, \textbf{cells}$ (marked by a black circle). When the value of $\bar{K}$ is below this threshold, the system has no PFPs, resulting in an uncontrollable tumor growth. Otherwise, when the value of $\bar{K}$ is above the threshold, the system has two PFPs, denoted by M^+ and M^- (Eq. (9)).

changes sign, is defined by the intersection of the characteristic polynomial with $\lambda = 0$

$$P(\lambda = 0, \bar{\Delta}_2 = \bar{\Delta}_{2_{crit}}) = 0. \tag{21}$$

Substitution of Eq. (17) in Eq. (21) yields

$$\bar{\Delta}_{2_{crit}} = \mu_A \cdot \mu_e \cdot \bar{\Delta}_1. \tag{22}$$

To prove necessity, assume that Eq. (20) is violated. As shown in Fig. 4c, when $\frac{dP(\lambda, \bar{\Delta}_2 = 0)}{d\lambda}|_{\lambda=0} < 0$ and $\bar{\Delta}_2 = 0$ the largest polynomial zero is positive and the rest are negative, similarly to the condition
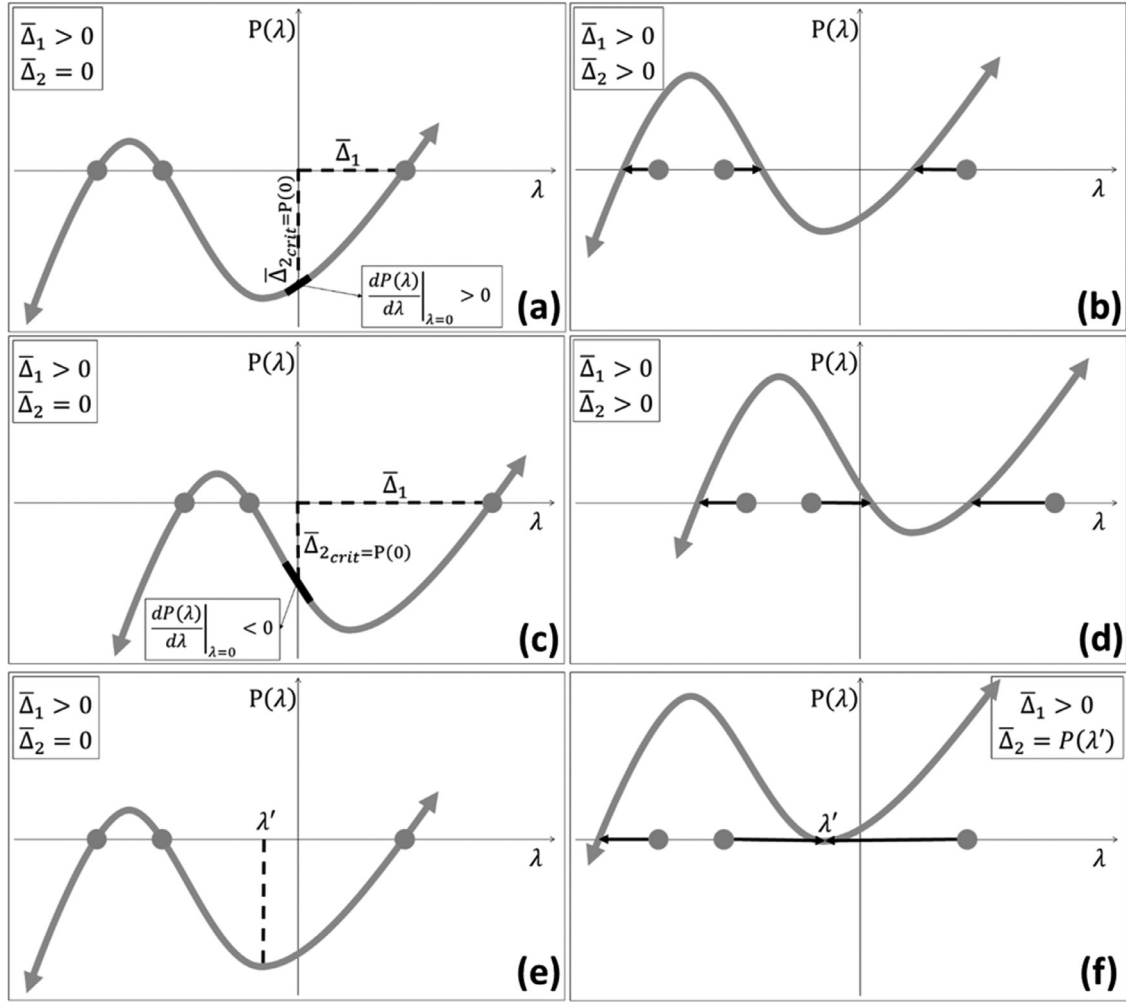
Fig. 4. Negativity of the real parts of the zeros of $P(\lambda)$ from Eq. (17) depends on its slope at $\lambda = 0$, and the values of $\bar{\Delta}_1$ and $\bar{\Delta}_2$ (Eq. (18)). The circles represent the zeros, λ of $P(\lambda, \bar{\Delta}_2 = 0)$. The largest zero is $\lambda = \bar{\Delta}_1$. a, c, and e show three different types of polynomials which satisfy $\bar{\Delta}_1 > 0$, according to Eq. (19), and $\bar{\Delta}_2 = 0$. These polynomials have two negative and one positive zeros. b, d, and f demonstrate a sign change of one of the zeros of $P(\lambda)$ in (4a), (4c), and (4e), respectively, when $\bar{\Delta}_2$ increases. First, the polynomial in (4a) intersects $\lambda = 0$ on the right side of its local minimum, thus satisfying $\frac{dP(\lambda)}{d\lambda}|_{\lambda=0} > 0$. If $\bar{\Delta}_2 > 0$ the largest zero approaches the origin until it becomes negative for $\bar{\Delta}_2 \geq \bar{\Delta}_{2_{crit}}$ (4b). In this case, all zeros have negative real parts and therefore the corresponding FP is stable. In contrast, if the intersection of $P(\lambda)$ with $\lambda = 0$ lies left of the local minimum, as shown in (4c), and if $\bar{\Delta}_2 > 0$, the second large zero changes sign from negative to positive (4d). Hence, either one or two zeros have a positive real part and therefore the corresponding FP is unstable. Lastly, zeros can become complex, as shown in (4e) and (4f). Consider for instance the local minimum on $\lambda = \lambda\prime$, shown in (4e). For $\bar{\Delta}_2 = \lambda\prime$ the two closest zeros to the minimum coincide and become a complex conjugate for $\bar{\Delta}_2 > \lambda\prime$, as shown in (4f). Sign determination of their real part is graphically not possible and further analytical and numerical calculations are required (see also Section 3.2.1).

in Fig. 4a. A larger value of $\bar{\Delta}_2$ shifts the polynomial upwards, but here the largest zero remains positive and the second biggest one becomes positive (Fig. 4d). Together, both conditions in Eq. (20) are therefore necessary and sufficient for local stability of a PFP with corresponding real eigenvalues. □

We next determined the parameter ranges for which Eq. (20b) is satisfied, in order to express the stability conditions in terms of the parameter space. We differentiate Eq. (17) and substitute $\lambda = 0$, as follows

$$\frac{dP(\lambda, \bar{\Delta}_2 = 0)}{d\lambda}\bigg|_{\lambda=0} = \mu_A \cdot \mu_e - \bar{\Delta}_1 \cdot (\mu_A + \mu_e). \tag{23}$$

Thus, the second necessary parametric condition for stability of a PFP is

$$\bar{\Delta}_1 < \frac{\mu_A \cdot \mu_e}{\mu_A + \mu_e}. \tag{24}$$

Under the estimated parameter values from Table 1, the r.h.s of Eq. (24) equals about 10 d^{-1}, and the value of $\bar{\Delta}_1$ is about 0.05 d^{-1}. Since according to Eq. (19a), the maximum value of $\bar{\Delta}_1$ is γ_{mel}

(0.08664 d^{-1}), Eq. (24) always holds, and thereby the stability condition in Eq. (20b) is always satisfied in the parameter ranges in Table 1. In conclusion, increase in the activation rate of CD8 T cells, reduction of their exhaustion rate, as well as low tumor growth rates enables stability of the corresponding PFP.

Claim 2. If a pair of PFPs of Eq. (1) has only real eigenvalues and if the condition in Eq. (20b) is satisfied, the larger PFP (with a larger value of M^*) is always unstable and the smaller one is always LAS.

Proof of Claim 2. Substitution of $\bar{\Delta}_1$, $\bar{\Delta}_2$, and $\bar{\Delta}_{2_{crit}}$ expressions from Eqs. (18) and (22) in the first necessary condition (Eq. (20a)) yields

$$\frac{b}{M^* + b} > \frac{M^*}{M^* + g}. \tag{25}$$

Simplifying it we get

$$M^{*2} < bg. \tag{26}$$

Substitution of M^{*2} from Eq. (8) in Eq. (26) yields

$$M^* < -\frac{2bg}{b+g-\bar{K}}. \tag{27}$$

In order to determine the stability of each FP in a system with two FPs, we substitute M^* from Eq. (9) into Eq. (27):

$$\pm\sqrt{\left(b+g-\bar{K}\right)^2 - 4b\cdot g} < -\frac{4b\cdot g}{b+g-\bar{K}} - \bar{K} + (b+g). \tag{28}$$

The r.h.s of Eq. (28) can be written as:

$$-\frac{4b\cdot g}{b+g-\bar{K}} - \bar{K} + (b+g) = \frac{\left(b+g-\bar{K}\right)^2 - 4b\cdot g}{b+g-\bar{K}}. \tag{29}$$

Substitution of Eq. (29) into Eq. (28) yields:

$$\pm\sqrt{\left(b+g-\bar{K}\right)^2 - 4b\cdot g} < \frac{\left(b+g-\bar{K}\right)^2 - 4b\cdot g}{b+g-\bar{K}}. \tag{30}$$

According to Eq. (14), the r.h.s of Eq. (30) is negative, and therefore this inequality is never satisfied for a plus sign in the l.h.s. Therefore, the necessary condition in Eq. (20a) does not hold for the larger PFP, M^+, indicating that it is always unstable.

For the lower PFP, M^-, we multiply both sides of Eq. (30) with -1 and square it:

$$1 > 1 - \frac{4b\cdot g}{\left(b+g-\bar{K}\right)^2}. \tag{31}$$

According to Eq. (31), the necessary condition in Eq. (20a) is always satisfied for M^-. Thus, if the second necessary condition in Eq. (20b) is satisfied always for M^-, the corresponding PFP is always stable. This claim implies that stability of the tumor depends on its size, and that large tumors are less likely to be stable. □

3.2.4. PFPs with complex eigenvalues are unstable in a treatment-free scenario but can be stable under ICI-increased immune efficacy.
Both stability conditions described by Eq. (20) relate to the case in which all zeros of the characteristic polynomial are real. However, the zeros can also be complex, with positive or negative real parts. We determined the parametric conditions for negativity of the real parts of complex zeros. As shown in Fig. 4e and Fig. 4f, two neighboring zeros can collide, subsequently becoming a conjugate complex pair (when $\bar{\Delta}_2$ becomes larger than the local minimum value of the characteristic polynomial with $\bar{\Delta}_2 = 0$, which lies between these zeros; marked by λ' in Fig. 4e). Due to the continuity of root values in the polynomial coefficients, and since the condition in Eq. (20b) is always satisfied under the estimated parameter values, when the conjugate complex pair is close to λ', its real parts are negative. However, for certain parameter values the real parts may change sign, namely, the system undergoes Hopf bifurcation (Hassard et al., 1981). The biological meaning of this is that tumors, whose system parameters correspond to negative real parts of all the eigenvalues of the Jacobi matrix, can be stabilized, while tumors, whose eigenvalues in the corresponding mathematical system have positive real parts, are unstable.

Since an explicit solution of the characteristic polynomial in its general form is hard to obtain, determination of the sign of the real part of the zeros is not always possible. Therefore, derivation of the stability conditions in this case requires further analysis, for example, by the application of the Hurwitz-Routh stability criterion (Brauer and Nohel, 2012; Yang, 2002; Liu, 1994; Douskos and Markellos, 2015) and numerical calculation of the eigenvalues of the Jacobi matrix. Here, we analytically determined the conditions for a Hopf bifurcation in the system at hand.

Consider a general form of a 3rd order characteristic polynomial with one negative real zero $\lambda = -\lambda_0$, where $\lambda_0 > 0$, and one conjugate pair of complex zeros $\lambda_1 \pm i\omega_1$, where $\omega_1 > 0$. The corresponding system undergoes a Hopf bifurcation when the real parts of the

two corresponding zeros are simultaneously zeroed, that is $\lambda_1 = 0$. The general form of the characteristic polynomial is then:

$$(\lambda + i\omega_1)\cdot(\lambda - i\omega_1)\cdot(\lambda + \lambda_0) = 0. \tag{32}$$

Opening parenthesis yields:

$$\lambda^3 + \lambda^2\cdot\lambda_0 + \lambda\cdot\omega_1^2 + \lambda_0\cdot\omega_1^2 = 0. \tag{33}$$

The necessary conditions for a Hopf bifurcation are deduced from the conditions on the polynomial coefficients (b_i):

$$\begin{aligned}
b_0 &= \lambda_0\cdot\omega_1^2 > 0, \\
b_1 &= \omega_1^2 > 0, \\
b_2 &= \lambda_0 > 0, \\
b_3 &= 1.
\end{aligned} \tag{34}$$

According to Eq. (34), a Hopf bifurcation exists in our system when all the coefficients of the characteristic polynomial in Eq. (17) are positive.

These coefficients are summarized here:

$$\begin{aligned}
b_0 &= \bar{\Delta}_2 - \bar{\Delta}_{2_{crit}}, \\
b_1 &= \mu_A\cdot\mu_e - \bar{\Delta}_1\cdot(\mu_A + \mu_e), \\
b_2 &= \mu_A + \mu_e - \bar{\Delta}_1, \\
b_3 &= 1.
\end{aligned} \tag{35}$$

The first and second coefficients in Eq. (35) are positive when Eqs. (20a) and (20b) are satisfied. Positivity determination of b_2 under consideration that $\bar{\Delta}_1 > 0$ yields the remaining condition for a Hopf bifurcation:

$$\begin{aligned}
b_2 &= \mu_A + \mu_e - \bar{\Delta}_1 > 0, \text{ or} \\
\bar{\Delta}_1 &< \mu_A + \mu_e.
\end{aligned} \tag{36}$$

Under realistic assumptions on the immune system's parameters (see Table 1), $\mu_A + \mu_e$ is approximately 0.4 d^{-1}. Since according to Eq. (19a), the maximum value of $\bar{\Delta}_1$ is $\gamma_{mel} \approx 0.004\,d^{-1}$, Eq. (36) is always satisfied, and therefore a Hopf bifurcation takes place for all parameter values. Significant reduction of the exhaustion rates, namely, μ_A, and μ_e, for example under treatment with ICI, can violate Eq. (36), and impose stability on the corresponding PFP, as well as the tumor size.

The condition we deduced in above is a consequence of the Ruth Horowitz criterion. The corresponding Routh array of the polynomial is:

b_3	b_1	0
b_2	b_0	0
$\frac{b_1\cdot b_2 - b_0\cdot b_3}{b_2}$	0	0
b_0	0	0

According to the Routh Horowitz criterion for stability of the corresponding FP, $b_i > 0$ must hold, as well as that all the terms in the left column of the Routh array must be positive. Here, the first, second, and fourth terms are positive. Substituting $b_3 = 1$ in the third term yields $\frac{b_1\cdot b_2 - b_0}{b_2}$. In the polynomial of Eq. (33), the real parts of the complex roots are zero, and therefore $\frac{b_1\cdot b_2 - b_0}{b_2} = 0$, namely $b_1\cdot b_2 = b_0$, and the complex roots are $\lambda = \pm i\sqrt{b_1}$. The condition of stability of the corresponding FP is

$$b_1\cdot b_2 - b_0 > 0 \tag{37}$$

Substituting b_i from Eq. (35) yields

$$\begin{aligned}
&\mu_A\cdot\mu_e\cdot\left(\mu_A + \mu_e - \gamma_{mel}\cdot\frac{b}{M+b} - 2\cdot\bar{\Delta}_1\right) \\
&+ (\mu_A + \mu_e)\cdot\bar{\Delta}_1\cdot\left(\bar{\Delta}_1 - 1\right) > 0
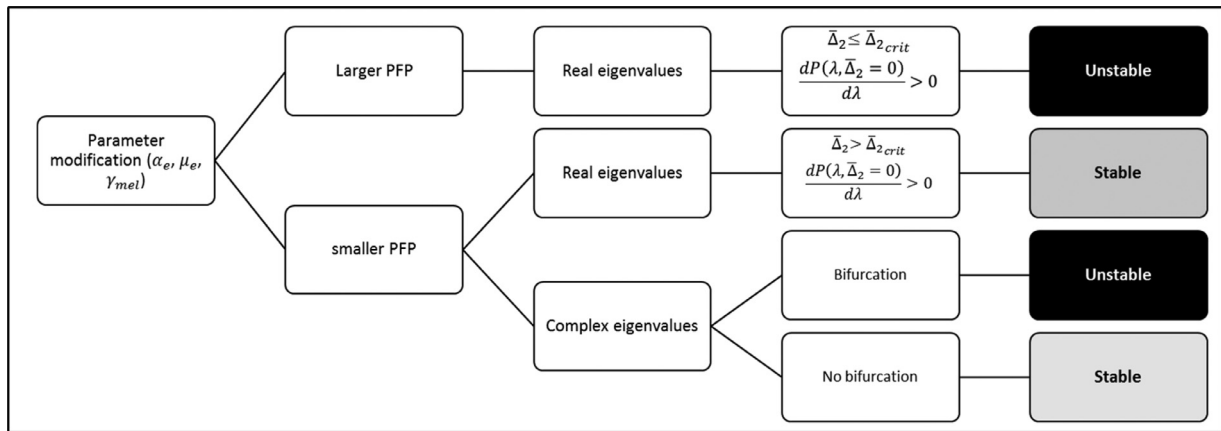\end{aligned} \tag{38}$$

Fig. 5. Summary of the local stability analysis of systems with two PFPs. The parameters α_e, μ_e, and γ_{mel} stand for the activation rate of CD8+ T cells, their exhaustion rate, and the tumor growth rate, respectively. The coefficients $\bar{\Delta}_2$, $\bar{\Delta}_{2_{crit}}$, and the function $P(\lambda)$ are defined in Eqs. (17), (18), and (22).

3.3. Stability of PFPs is linked to a small tumor burden and an enhanced activation of CD8+ T cells. For a better understanding of the local stability patterns, we numerically calculated FPs and the corresponding eigenvalues for 62,500 parameter sets. In each set, we modified the values of α_e, and μ_e, specified in Table 1, from 1 to 9000 fold, and 1/9000 to 1 fold, respectively. We chose to focus on changes in α_e, and μ_e due to their direct effect on the number of CD8+ T cells in the host. We also examined the effect of the tumor growth rate on the local stability of the FPs by repeating the above numerical analysis for both the minimal and the maximal estimated value of γ_{mel} in Table 1. The rest of the parameters remained unchanged from their reference values in Table 1. For each parameter set we determined the stability of each corresponding FP by numerical calculation of the eigenvalues of Eq. (17). We recorded an FP as locally asymptotically stable, if all real parts of its corresponding eigenvalues were negative. Otherwise, we flagged the FP as unstable. The results of these computations, are listed below (see also Fig. 5).

1. **In a system with two PFPs, the larger PFP is unstable over the whole range of α_e, μ_e, and γ_{mel}.** The numerical analysis indicated that the two PFPs have a single real-positive eigenvalue over the examined range of α_{pri}, μ_e, and γ_{mel}. The rest of the eigenvalues can be real or complex, all having negative real parts (not shown).
2. **Increase in the activation rate of CD8+ T cells, α_e , leads to local stability of the smaller PFP, while reduction in the exhaustion rate of CD8+ cells, μ_e, leads to local instability.** Under the minimal and maximal values of γ_{mel} from Table 1, locally stable FPs are associated with low values of μ_e, and relatively large values of α_e. In addition, the FPs under the minimal value of γ_{mel} have higher stability when compared to those under the maximal value of γ_{mel}.
3. **Instability of the smaller PFP in a system with two PFPs is due to positive real parts of a single conjugate pair of complex eigenvalues.**

All analyzed unstable FPs have positive real parts of only complex eigenvalues.

Fig. 5 summarizes the results of both the theoretical and the numerical local stability analyses. One can see in this summary that the larger PFP is always unstable, while the smaller one is unstable only when the corresponding Jacobi matrix has two complex eigenvalues with real parts, which change sign due to Hopf bifurcation.

3.4. Phase-plane analysis emphasizes the role of the initial tumor burden in converging towards a stable PFP, and reveals oscillations around an unstable PFP

We next studied the global dynamics of the system by a phase-plane analysis, in order to study the dynamics of the cell populations away from the PFPs. To this end, we plotted the time course of the values of the two most relevant variables, effector CD8+ T cells (T) and tumor cells (M), versus each other. Representative phase portraits of the system, having zero, one, or two FPs are shown and explained in the following paragraphs. The simulation results are summarized in Fig. 6.

No PFPs

Under the estimated parameters from Table 1, the system has no PFPs. As shown in Fig. 6a, the number of tumor cells in this case grows uncontrollably, while the number of effector CD8+ T cells eventually reaches saturation.

A single PFP

As previously shown in Figs. 2 and 3, for certain parameter values, the condition in Eq. (13) is satisfied and the system has a single PFP. In the particular phase portrait shown in Fig. 6b, the obtained FP is a saddle node, which refers to a consolidation of a stable and an unstable FP. The part of this phase portrait, for which the initial number of tumor cells is less than 5×10^6, constitutes the basin of attraction. All trajectories, beginning inside this basin of attraction, converge to the FP, while all trajectories beginning with a larger number of tumor cells diverge away from this point. The biological implication of this is that tumors with initially less than 5×10^6 cells will stabilize.

Two PFPs

Depending on the parameter values, the system can have two PFPs. Exemplary phase portraits of such systems are shown in Fig. 6c–e. Each of these systems has different parameters, but the same value of $\bar{K}$ and the same number of tumor cells in steady state. We found that modification of α_e, and μ_e can induce oscillatory changes in the number of tumor cells. First, as shown in Fig. 6c, increasing the activation rates of CD8+ T cells generates a locally stable PFP and an unstable PFP. If the initial size of the tumor cell population is located within the basin of attraction of the smaller PFP, the number of tumor cells approaches this point with damped oscillations and the disease becomes stable. However, if the initial size of the tumor cell population is located outside the basin of attraction, the corresponding trajectory escapes from the larger PFP, which results in an uncontrollable tumor growth and disease progression. Secondly, as shown in Fig. 6d, reducing the exhaustion rate of CD8+ T cells generates two PFPs. The number of tumor cells around the smaller FP undergoes increasing oscillations.
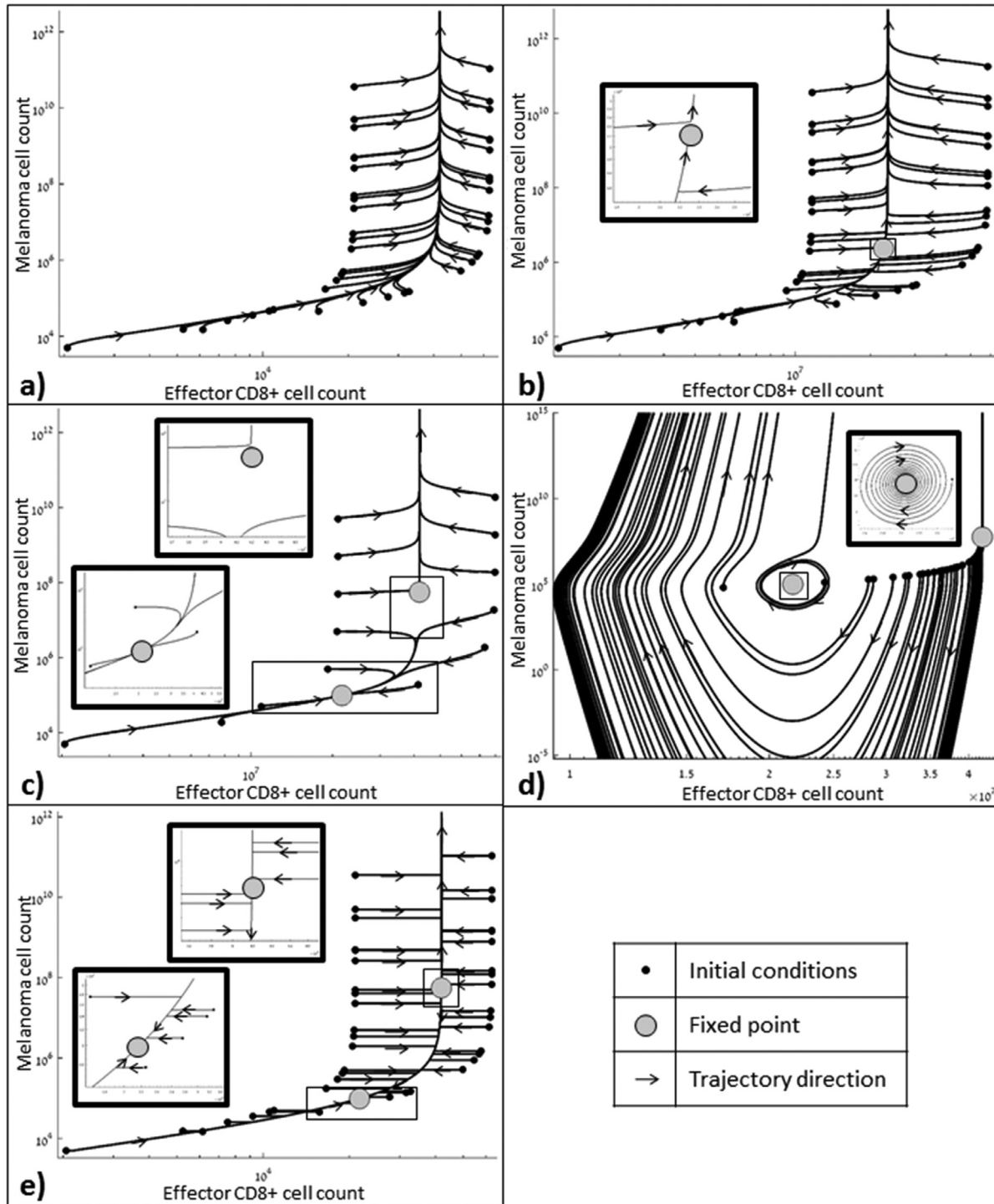
Fig. 6. Phase plane analysis captures disease control for an initially low tumor burden. Here we show representative phase planes of the 3-dimensional system described in Eq. (1), which are projected here on the effector CD8+ T cells (T) – melanoma cells (M) plane. The black curves represent trajectories of $(T(t), M(t))$ and the small circles mark the initial points of each curve. Arrows mark the direction of the trajectories. Big circles denote FPs, at which the number of cells remains constant with time. It separates between different dynamic patterns of the cell populations. Information on the parameter values and initial number of cells is summarized in Table 3. a shows a phase portrait of a system with the parameter values estimated from the literature (Table 1); no FPs have been identified, indicating tumor escape and its eventual uncontrollable growth. b shows a phase portrait of a system with a single FP, (thin frame with a zoom in in the thick frame). This point is marked by a black circle in Fig. 3. Initially large tumors grow in size, while initially small tumors evolve to be limited by the immune system. As shown in (b), starting from initial number of about 10^7 tumor cells results in different fates of the tumor dynamics. Figure 6c-e represent phase planes of different systems with two FPs, characterized by different parameter values. (c) Increased α_e generates curved trajectories which tend to the lower FP. This indicates short oscillations (stable focus; thin frame with a zoom-in within the thick frame). Trajectories with the initial number of cancer cells larger than ~5×10^6 escape from the larger FP (unstable focus; thin frame with a zoom in in the thick frame). (d) Reduced value of μ_e leads to spiral trajectories, spiraling away from a FP, which indicates growing oscillations. Interestingly, trajectories, which begin close to this FP (thin frame) are attracted to it, as zoomed in the thick frame. (e) Reduced value of γ_{mel} results in a non-oscillatory dynamics, such that trajectories, which begin with initially small number of tumor cells converge into a smaller stable focus and trajectories (lower thin frame with a zoom in in the lower thick frame), which begin with a larger number of tumor cells escape from a larger unstable focus (upper thin frame with a zoom in in the upper thick frame).

In some cases the amplitude is so large that the tumor will virtually disappear and then grow again, escaping from host immunity. When the initial number of cancer cells is close to the value at this FP, the system will eventually converge to this FP. When the initial number of cancer cells is close to the larger PFP, it will either escape from it towards the smaller PFP or grow uncontrollably. Thus, considering two similar sets of initial conditions, one mapping a point, located slightly above the larger PFP, and the other mapping a point, located slightly below this point, we note that each of these points evolves differently in time, corresponding to a different disease fate. The evolution of the first set leads to temporary shrinkage or tumor stability, while the evolution of the second set leads to disease progression (Fig. 6d, magnified area). In addition to the effects of the host immunity, reduction of the tumor growth rate also leads to generation of PFPs in the system. As shown in Fig. 6e, reducing the value of γ_{mel} leads to a sharp, non-oscillatory decay in the number of tumor cells towards the smaller PFP, or escape from the larger FP (Fig. 6e), depending on the initial number of tumor cells.

To better visualize the outcome of the model simulation for each steady state, we chose representative initial conditions around the smaller PFP for each steady state shown in Fig. 6c and d, and plotted time series of the corresponding trajectories (Fig. 7). It can be seen that under a reduced exhaustion rate of CD8+ T cells, the tumor size oscillates around the smaller PFP. As the initial conditions get closer to this FP, the frequency of the oscillations increase (Fig. 7b–d). Their amplitude decays and then stabilizes very close to this FP, while increasing in trajectories that are further away from the smaller PFP.

The dynamic patterns of tumor growth, shown in Fig. 7, correspond to different types of response to immunotherapy. We note in Fig. 7a, that an increase in the activation rate of CD8+ T cells due to treatment, stabilizes the tumor size within a period of a few months. The larger the activation rate gets, the smaller is the corresponding tumor size at steady state, and the larger is the basin of attraction of this stable FP. On the other hand, patients whose therapy leads to significant reduction in death rates of immune cells (Fig. 7b–d) can experience different disease fates, depending on the ratio between the activation and the exhaustion rates of CD8+ T cells, as well as on the initial number of tumor cells, and on the number of immune cells. For large ratios between the activation and the exhaustion rates of CD8+ T cells, the value of $\bar{\Delta}_2$ is large enough for two neighboring polynomial zeros to coincide and form a complex-conjugate pair (Fig. 4e and f). This results in a period of oscillatory tumor dynamics, followed by stability of tumor size or an uncontrollable growth. Under the initial number of tumor and immune cells lying in the closest trajectory to the smaller FP, the oscillations decay, leading to a stable tumor size (Fig. 7b). In contrast, on a different trajectory, which starts further from this FP, the corresponding tumor size oscillates for a while, followed by an uncontrollable growth (Fig. 7c). Away from a stable PFP, and when the initial number of CD8+ T cells is larger than its number at steady state, the tumor shrinks considerably, only to reappear after about a decade (Fig. 7d). Taken together, these results suggest that when an immunotherapeutic intervention increases the activation rate of effector cells, immunotherapy will lead to disease stabilization. In contrast, when immunotherapy relieves the exhaustion of CD8+ T cells, the outcomes may vary from decaying oscillatory convergence, through a stable tumor size, to uncontrollable growth, depending on the initial conditions of the tumor and immune cells.

4. Discussion

In this article we showed by mathematical modeling and analysis within the bio-medically relevant parameter ranges, that the ratio between activation and exhaustion rates of CD8+ T cells can determine the outcomes of melanoma immunotherapy. Based on our results, we suggest to evaluate T cell activation and exhaustion rates in individual patients for improving the prediction accuracy of their response to treatment.

Our theoretical and numerical analyses suggest that under realistic assumptions on tumor growth and immune efficacy in an untreated person, the cancer always evades the control of the immune system, and, indeed, spontaneous regression of melanoma is rarely observed (Everson, 1964). However, our analysis also indicates that under immunotherapy with ICI, which causes increased activation or decreased mortality of effector CD8+ T cells, stabilization of the tumor size is possible. Increased activation of effector CD8+ T cells has been clinically observed in response to immunotherapy. For instance, vaccination of melanoma patients with a LAG-3 antibody resulted in enhanced proliferation of tumor-specific CD8+ T cells in 13 out of 16 patients (Legat et al., 2016). Similar findings were made also in non-small-cell lung cancer, with a proliferative burst of effector PD-1+CD8+ T cells observed in 70% of the patients upon treatment with anti-PD-1 (Kamphorst et al., 2017). Furthermore, analysis of melanoma biopsies from 46 patients, before and during anti-PD-1 treatment shows an increase in the proliferation of intra-tumor PD-1++CD8+ T cells following treatment (Tumeh et al., 2014). Association of therapy outcomes with ICI-caused CD8+ T cell proliferation was examined in the clinical setting, observing enhanced and early proliferation, mostly among responders (Kamphorst et al., 2017; Tumeh et al., 2014; Huang et al., 2017). However, samples from some responders did not show increased proliferation of CD8+ T cells. Clearly, then, it is not sufficient to measure the activation rate of CD8+ T cells for accurately predicting the ICI outcomes. Integrating in the model also the impact of CD8+ T cells on the tumor can improve the prediction accuracy of the personal response.

Our results indicate that extended periods of disease stability can result from increased activation of immune cells, while oscillatory tumor growth is induced by reduced exhaustion of the immune cells, for example, due to immunotherapy. From this finding we infer that immunotherapy by ICI could yield different patterns of change in the disease burden. The amplitude of the modeled oscillations is in the order of 10^6 cells. Considering that a tumor lesion with 1 cm diameter comprises about 10^9 cells (Del Monte, 2009), and that a lesion is confidently measurable if its diameter is at least 1 cm (Eisenhauer et al., 2009), the oscillations are most likely averaged out in clinical size assessments. Still, small oscillations in the size of tumor and immune cells have been previously suggested. For example, Coventry et al. (Coventry et al., 2009) measured the levels of C-reactive protein (CRP) in patients with melanoma and other cancer indications, and for most cases reported oscillatory patterns, with periodicity of 6–7 days. These oscillations were linked to changes in the disease intensity and strength of inflammatory signatures. The authors suggest that tumor cells induce infection, which leads to a deficit of T cells, and, subsequently, to their increased proliferation. The effector cells, in turn, eliminate tumor cells. Other tumor cells proliferate rapidly, thereby driving the feedback between immune cells and cancer cells. Of note, similar feedback was discussed by d'Onforio et al., (d'Onofrio et al., 2010), who applied a family of mathematical models to analyze tumor-immune interactions. In their study, d'Onforio et al., analyzed the effect of time delays between the tumor size at a given moment and its effect on the stimulation of immune effector cells. They show that exponentially distributed time delays can induce sustained oscillations in the number of cells. Correspondingly, the oscillation observed in our study can be explained by an exponentially distributed time lag between the tumor-induced stimulation term in Eq. (1a), namely $\alpha_A \cdot \frac{M}{M+b}$, and oscillations in the number of functional APCs, $A(t)$.
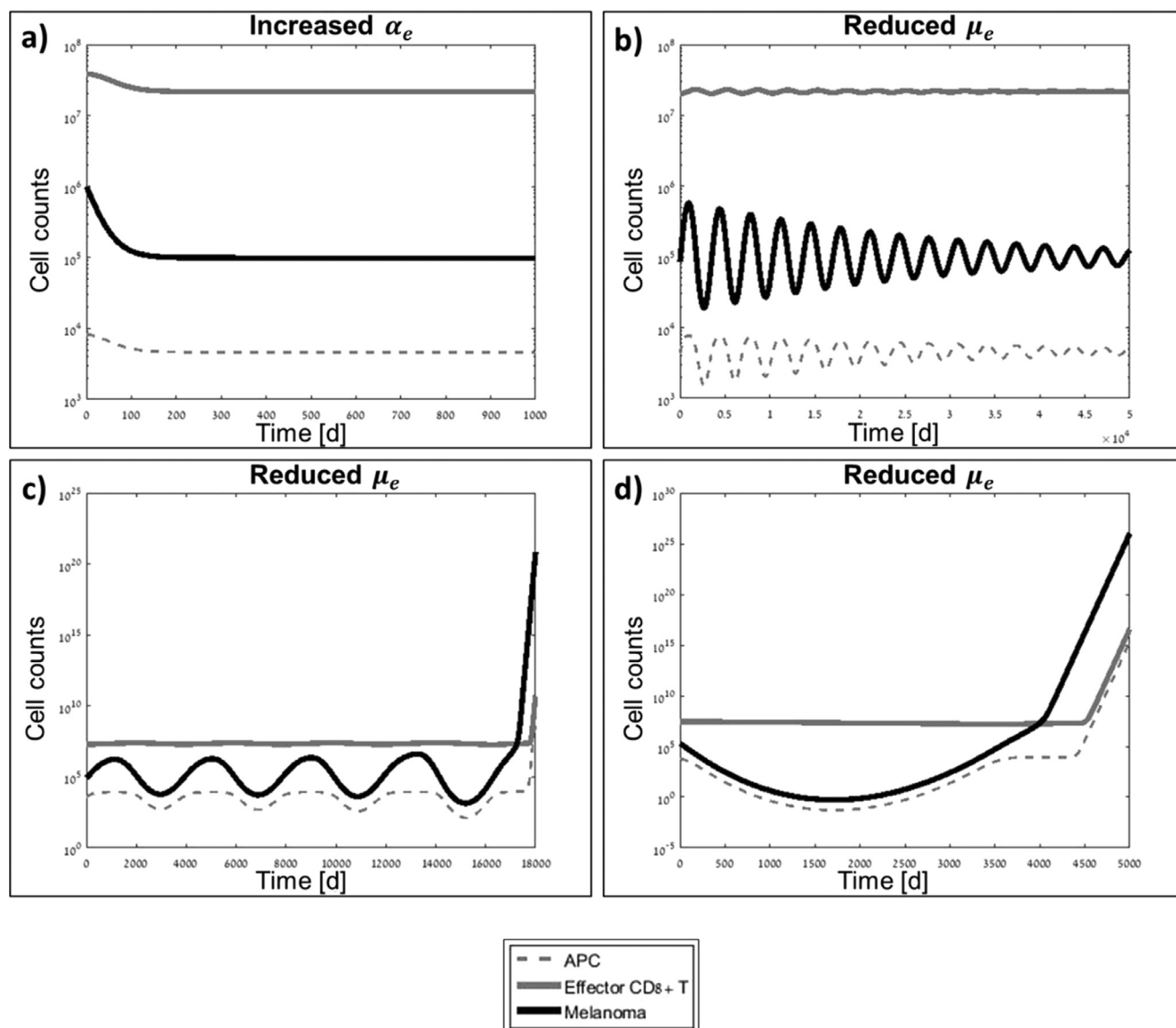
Figure	Initial number of melanoma cells
(a)	10^6
(b)	$8.5 \cdot 10^4$
(c)	$8 \cdot 10^4$
(d)	$2 \cdot 10^5$

Fig. 7. Representative time series for the number of immune and tumor cells around the fixed points; a and b–d are plotted for the same parameter sets in the phase portraits as in Fig. 6c and d, respectively. The initial number of immune cells was set under assumption of quasi-steady state, that is, the number of immune cells adjusts itself to the number of tumor cells, according to Eq. (5).

Our analysis emphasizes the effect of tumor growth rate and baseline tumor burden on the success of immunotherapy. Tumor shrinkage is possible only if the initial number of tumor cells, and the initial number of immune cells are located within the basin of attraction of the lower PFP. For patients with a significantly larger initial tumor burden, a larger effect of the checkpoint blockade is required to induce tumor shrinkage. From a mathematical point of view, as the immune efficacy increases, the ratio between the efficacy of the immune response and the tumor growth rate increases, which, as shown in Fig. 3, leads to a larger difference between both FPs, and thus a larger basin of attraction of the stable FP. These results imply that patients with initially small tumor burden should benefit more from this therapy, supporting reports that high tu-

mor burden is associated with poorer outcome to ICI (Joseph et al., 2018; Ribas et al., 2016; Robert et al., 2017). Based on our results, we suggest to clinically test the effect of adjuvant therapy with ICI. We believe that the reduction of tumor load, either by resection or by radiation, prior to treatment by ICI, will augment the clinical benefit of ICI-based therapy. Interestingly, the benefit of combining immunotherapy and resection, but in an inverse sequence to the one suggested here, was clinically shown in a study reporting that administration of pembrolizumab as an adjuvant therapy for patients with completely resected high-risk stage III melanoma increased the recurrence-free survival of treated patients, as compared to patients who received placebo (Eggermont et al., 2018). Support for our model findings on the relation between immune

cell activity and initial tumor load can be found in (Huang et al., 2017). Huang and colleagues checked a combined emergent parameter - the ratio between the reinvigoration rate of CD8+ T cells (as measured by the percentage of CD8+ T cells expressing Ki67) and the tumor burden at baseline, and correlated this ratio with the observed clinical response of patients to pembrolizumab. Their conclusion is that the combined ratio can better distinguish clinical outcomes and predict response than each one of these parameters taken alone, and that this ratio can serve as a calibrated parameter, predicting response to PD-1 blockade.

To facilitate the mathematical analyses, our model was deliberately kept simple, taking into account only the main effects of pembrolizumab on CD8+ T cells and the melanoma tumor. In particular, the effects of treatment were modeled by assigning bigger or smaller values to the activation rate of CD8+ T cells, α_e, and to the elimination rate, μ_e. The immune system as well as the consequences of ICI-based therapy are obviously far more complex. For example, the mechanism of action of pembrolizumab includes effects on interactions with additional cell populations, such as myeloid-derived suppressor cells (MDSCs), natural killer cells (NK), and helper CD4+ T cells (Nguyen and Ohashi, 2015). Similarly to CD8+ T cells, NK cells have a cytotoxic effect on tumor cells. Since they express PD-1, treatment with pembrolizumab may increase the abundance of functional NK cells, and thereby also contribute to the tumor growth control (Beldi-Ferchiou and Caillat-Zucman, 2017). Moreover, cytometric analysis of blood samples from patients with advanced melanoma under pembrolizumab and nivolumab show that the anti-PD-1 treatment reduces the frequency of circulating MDSCs, and increases the frequency of circulating NK cells among responders (De Coaña et al., 2018). Such additional processes can be considered for inclusion in the model in future extensions.

In summary, our study provides new insight into the interactions between the immune system and melanoma, enabling a better understanding of the potential response of individual patients with metastatic melanoma to ICI treatment. Analysis of our mechanistic model showed that while the natural immunity is not sufficient to control the growth of melanoma tumors in the absence of treatment, administration of ICIs can turn the uncontrollable tumor growth into shrinkage or stabilization, depending on the individual patient characteristics. This can provide a basis for future studies in which model-based predictors for response to ICI treatment could be developed to address the need for improved and personalized prognosis in melanoma.

Acknowledgments

References

Adam, J., Bellomo, N., 2012. A Survey of Models for Tumor-Immune System Dynamics. Springer Science & Business Media.

Agur, Z., et al., 2016. Employing dynamical computational models for personalizing cancer immunotherapy. Expert Opin. Biol. Ther. 16 (11), 1373–1385.

Barrio, M.M., et al., 2012. Human macrophages and dendritic cells can equally present MART-1 antigen to CD8+ T cells after phagocytosis of gamma-irradiated melanoma cells. PLoS One 7 (7), e40311.

Beldi-Ferchiou, A., Caillat-Zucman, S., 2017. Control of NK cell activation by immune checkpoint molecules. Int. J. Mol. Sci. 18 (10), 2129.

Bossi, G., et al., 2013. Examining the presentation of tumor-associated antigens on peptide-pulsed T2 cells. Oncoimmunology 2 (11), e26840.

Brauer, F., Nohel, J.A., 2012. The Qualitative Theory of Ordinary Differential Equations: an Introduction. Courier Corporation.

Butte, M.J., et al., 2007. Programmed death-1 ligand 1 interacts specifically with the B7-1 costimulatory molecule to inhibit T cell responses. Immunity 27 (1), 111–122.

Carlson, J.A., 2003. Tumor doubling time of cutaneous melanoma and its metastasis. Am. J. Dermatopathol. 25 (4), 291–299.

Chapon, M., et al., 2011. Progressive upregulation of PD-1 in primary and metastatic melanomas associated with blunted TCR signaling in infiltrating T lymphocytes. J. Invest. Dermatol. 131 (6), 1300–1307.

Chen, L., et al., 1994. Tumor immunogenicity determines the effect of B7 costimulation on T cell-mediated tumor immunity. J. Exp. Med. 179 (2), 523–532.

Cipponi, A., et al., 2011. Tumor-infiltrating lymphocytes: apparently good for melanoma patients. But why? Cancer Immunol. Immunother. 60 (8), 1153–1160.

Coventry, B.J., et al., 2009. CRP identifies homeostatic immune oscillations in cancer patients: a potential treatment targeting tool? J. Transl. Med. 7 (1), 102.

d'Onofrio, A., et al., 2010. Delay-induced oscillatory dynamics of tumour–immune system interaction. Math. Comput. Modell. 51 (5-6), 572–591.

d'Onofrio, A., 2005. A general framework for modeling tumor-immune system competition and immunotherapy: mathematical analysis and biomedical inferences. Physica D 208 (3-4), 220–235.

d'Onofrio, A., 2008. Metamodeling tumor–immune system interaction, tumor evasion and immunotherapy. Math. Comput. Modell. 47 (5), 614–637.

De Coaña, Y.P., et al., 2018. Abstract LB-116: Myeloid derived suppressor cells and NK cells are correlated with clinical benefit and survival in advanced melanoma patients treated with PD-1 blocking antibodies nivolumab and pembrolizumab. In: Proceedings of the American Association for Cancer Research Annual Meeting 2018; 2018 Apr 14-18; Chicago, IL. Philadelphia (PA): AACR; Cancer Res 2018;78(13 Suppl): Abstract nr LB-116.

de Vries, I.J.M., et al., 2003. Effective migration of antigen-pulsed dendritic cells to lymph nodes in melanoma patients is determined by their maturation state. Cancer Res. 63 (1), 12–17.

de Vries, I.J.M., et al., 2005. Magnetic resonance tracking of dendritic cells in melanoma patients for monitoring of cellular therapy. Nat. Biotechnol. 23 (11), 1407–1413.

Del Monte, U., 2009. Does the cell number 109 still really fit one gram of tumor tissue? Cell Cycle 8 (3), 505–506.

Douskos, C., Markellos, P., 2015. Complete coefficient criteria for five-dimensional hopf bifurcations, with an application to economic dynamics. J. Nonlinear Dyn. vol. 2015, Article ID 278234, 11 pages, 2015. https://doi.org/10.1155/2015/278234 2015.

Dustin, M.L., 2002. The immunological synapse. Arthritis Res. 4 (Suppl 3), S119–S125.

Dustin, M.L., 2014. The immunological synapse. Cancer Immunol. Res. 2 (11), 1023–1033.

Eftimie, R., Gillard, J.J., Cantrell, D.A., 2016. Mathematical models for immunology: current state of the art and future research directions. Bull. Math. Biol. 78 (10), 2091–2134.

Eggermont, A.M., et al., 2018. Adjuvant Pembrolizumab versus placebo in resected stage III melanoma. N. Engl. J. Med. 378 (19), 1789–1801.

Eisenhauer, E., et al., 2009. New response evaluation criteria in solid tumours: revised RECIST guideline (version 1.1). Eur. J. Cancer 45 (2), 228–247.

Eladdadi, A., Radunskaya, A., 2014. Modeling cancer-immune responses to therapy. J. Pharmacokinet. Pharmacodyn. 41 (5), 461–478.

Everson, T.C., 1964. Spontaneous regression of cancer. Ann. N. Y. Acad. Sci. 114 (2), 721–735.

Foryś, U., Bodnar, M., Kogan, Y., 2016. Asymptotic dynamics of some t-periodic one-dimensional model with application to prostate cancer immunotherapy. J. Math. Biol. 73 (4), 867–883.

Gattinoni, L., Klebanoff, C.A., Restifo, N.P., 2012. Paths to stemness: building the ultimate antitumour T cell. Nat. Rev. Cancer 12 (10), 671–684.

Hamid, O., et al., 2013. Safety and tumor responses with lambrolizumab (anti-PD-1) in melanoma. N. Engl. J. Med. 369 (2), 134–144.

Hassard, B.D., Kazarinoff, N.D., Wan, Y.-H., 1981. Theory and Applications of Hopf Bifurcation, 41. CUP Archive.

Hodi, F.S., et al., 2010. Improved survival with ipilimumab in patients with metastatic melanoma. N. Engl. J. Med. 363 (8), 711–723.

Huang, A.C., et al., 2017. T-cell invigoration to tumour burden ratio associated with anti-PD-1 response. Nature.

Joseph, W.L., Morton, D.L., Adkins, P.C., 1971. Variation in tumor doubling time in patients with pulmonary metastatic disease. J. Surg. Oncol. 3 (2), 143–149.

Joseph, R.W., et al., 2018. Baseline Tumor Size Is an Independent Prognostic Factor for Overall Survival in Patients With Melanoma Treated With Pembrolizumab. Clin. Cancer Res. 2386.2017 clincanres.

Kamath, A.T., et al., 2000. The development, maturation, and turnover rate of mouse spleen dendritic cell populations. J. Immunol. 165 (12), 6762–6770.

Kamphorst, A.O., et al., 2017. Proliferation of PD-1+ CD8 T cells in peripheral blood after PD-1–targeted therapy in lung cancer patients. In: Proceedings of the National Academy of Sciences.

Karimkhani, C., et al., 2017. The global burden of melanoma: results from the Global Burden of Disease Study 2015. Br. J. Dermatol. 177 (1), 134–140.

Kogan, Y., et al., 2012. Reconsidering the paradigm of cancer immunotherapy by computationally aided real-time personalization. Cancer Res. 72 (9), 2218–2227.

Kronik, N., et al., 2008. Improving alloreactive CTL immunotherapy for malignant gliomas using a simulation model of their interactive dynamics. Cancer Immunol. Immunother. 57 (3), 425–439.

Kronik, N., et al., 2010. Predicting outcomes of prostate cancer immunotherapy by personalized mathematical models. PLoS One 5 (12), e15482.

Kuznetsov, V., Zhivoglyadov, V., Stepanova, L., 1992. Kinetic approach and estimation of the parameters of cellular interaction between the immunity system and a tumor. Arch. Immunol. Ther. Exp. 41 (1), 21–31.

Kuznetsov, V.A., et al., 1994. Nonlinear dynamics of immunogenic tumors: parameter estimation and global bifurcation analysis. Bull. Math. Biol. 56 (2), 295–321.

Kuznetsov, V., 1990. A mathematical model for the interaction between cytotoxic T lymphocytes and tumour cells. Analysis of the growth, stabilization, and regression of a B-cell lymphoma in mice chimeric with respect to the major histocompatibility complex. Biomed. Sci. 2 (5), 465–476.

Lee, T.-H., Cho, Y.-H., Lee, M.-G., 2007. Larger numbers of immature dendritic cells augment an anti-tumor effect against established murine melanoma cells. Biotechnol. Lett. 29 (3), 351–357.

Legat, A., et al., 2016. Vaccination with LAG-3Ig (IMP321) and peptides induces specific CD4 and CD8 T-cell responses in metastatic melanoma patients—report of a phase I/IIa clinical trial. Clin. Cancer Res. 22 (6), 1330–1340.

Liu, W.-m., 1994. Criterion of Hopf bifurcations without using eigenvalues. J. Math. Anal. Appl. 182 (1), 250–256.

Nguyen, L.T., Ohashi, P.S., 2015. Clinical blockade of PD1 and LAG3 [mdash] potential mechanisms of action. Nat. Rev. Immunol. 15 (1), 45–56.

Ott, P.A., Hodi, F.S., Robert, C., 2013. CTLA-4 and PD-1/PD-L1 blockade: new immunotherapeutic modalities with durable clinical benefit in melanoma patients. Clin. Cancer Res. 19 (19), 5300–5309.

Prieto, P.A., et al., 2012. CTLA-4 blockade with ipilimumab: long-term follow-up of 177 patients with metastatic melanoma. Clin. Cancer Res. 18 (7), 2039–2047.

Ribas, A., et al., 2016. Association of pembrolizumab with tumor response and survival among patients with advanced melanoma. JAMA 315 (15), 1600–1609.

Rizvi, N.A., et al., 2015. Mutational landscape determines sensitivity to PD-1 blockade in non–small cell lung cancer. Science 348 (6230), 124–128.

Robert, C., et al., 2015. Pembrolizumab versus ipilimumab in advanced melanoma. N. Engl. J. Med.

Robert, C., et al., 2017. Durable complete response after discontinuation of pembrolizumab in patients with metastatic melanoma. J. Clin. Oncol. 6270 JCO. 2017.75.

Schumacher, T.N., Schreiber, R.D., 2015. Neoantigens in cancer immunotherapy. Science 348 (6230), 69–74.

Siegel, R.L., Miller, K.D., Jemal, A., 2018. Cancer statistics, 2018. CA Cancer J. Clin. 68 (1), 7–30.

Snyder, A., et al., 2014. Genetic basis for clinical response to CTLA-4 blockade in melanoma. N. Engl. J. Med. 371 (23), 2189–2199.

Tumeh, P.C., et al., 2014. PD-1 blockade induces responses by inhibiting adaptive immune resistance. Nature 515 (7528), 568–571.

Taylor, G.P., et al., 1999. Effect of lamivudine on human T-cell leukemia virus type 1 (HTLV-1) DNA copy number, T-cell phenotype, and anti-tax cytotoxic T-cell frequency in patients with HTLV-1-associated myelopathy. J. Virol. 73 (12), 10289–10295.

Terushkin, V., Halpern, A.C., 2009. Melanoma early detection. Hematol./Oncol. Clin. 23 (3), 481–500.

Von Euw, E.M., et al., 2007. Monocyte-derived dendritic cells loaded with a mixture of apoptotic/necrotic melanoma cells efficiently cross-present gp100 and MART-1 antigens to specific CD8+ T lymphocytes. J. Transl. Med. 5 (1), 19.

Walker, L.S., Sansom, D.M., 2011. The emerging role of CTLA4 as a cell-extrinsic regulator of T cell responses. Nat. Rev. Immunol. 11 (12), 852–863.

Wang, W., et al., 2012. Biomarkers on melanoma patient T cells associated with ipilimumab treatment. J. Transl. Med. 10 (1) 146–146.

Weide, B., et al., 2016. Baseline biomarkers for outcome of melanoma patients treated with pembrolizumab. Clin. Cancer Res. clincanres. 0127.2016.

Yang, X., 2002. Generalized form of Hurwitz-Routh criterion and Hopf bifurcation of higher order. Appl. Math. Lett. 15 (5), 615–621.